Available online at www.sciencedirect.com
SCIENCE DIRECT®
Combustion and Flame 138 (2004) 40–54
Combustion and Flame
www.elsevier.com/locate/jnlabr/cnf

Formation of charged aggregates of Al_2O_3 nanoparticles by combustion of aluminum droplets in air

V.V. Karasev [a], A.A. Onischuk [a,*], O.G. Glotov [a], A.M. Baklanov [a], A.G. Maryasov [a], V.E. Zarko [a], V.N. Panfilov [a], A.I. Levykin [b], K.K. Sabelfeld [b]

[a] *Institute of Chemical Kinetics and Combustion, Siberian Branch of the Russian Academy of Sciences, 630090, Novosibirsk, Russia*
[b] *Institute of Computational Mathematics and Mathematical Geophysics, Siberian Branch of the Russian Academy of Sciences, 630090, Novosibirsk, Russia*

Received 2 November 2003; received in revised form 24 February 2004; accepted 5 April 2004

Available online 4 May 2004

Abstract

The mechanism of Al_2O_3 nanoparticles aggregation in air was studied under atmospheric pressure conditions. Alumina nanoparticles were generated by combustion of a small sample of solid rocket propellant. Size and morphology of nanoparticles were studied by transmission electron microscopy. It was determined that alumina nanoparticles form aggregates of size about 1 μm composed of primary particles with a diameter of few tens of nm. The aggregates' coagulation was observed directly by a video system. In addition, the aggregate movement in the electric field was recorded by the video system. These observations showed that the majority of aggregates are charged. The typical aggregate charge is about 10 elementary units. Some aggregates are dipoles as indicated by the aggregate rotation when the electric field polarity is changed. The mechanism of aggregate formation has been proposed. The initial stage of alumina nanoparticle synthesis includes the formation of liquid oxide particles in the reaction zone located around the surface of burning Al droplet. When the particles pass to the relatively low-temperature region, solidification of particles occurs followed by clustering of solid spherical Al_2O_3 particles. Later, an aggregation of clusters formed by different burning Al droplets occurs resulting in formation of final aggregates. Estimations of thermal emission of electrons by the burning Al droplets were carried out via solution of the Poisson–Boltzmann equation. These estimates showed that the negative volume charge in the reaction zone around the Al droplet is 10^8–10^9 elementary charges per cm^3.

Keywords: Alumina; Nanoparticles; Aggregate; Electric charge; Fractal dimension

1. Introduction

The combustion of single Al particles in air at atmospheric pressure has been studied by several investigators; see the reference list in [1]. The main goal of the researches was to obtain data on Al global combustion characteristics, including the ignition delay, burning rate, and stability of combustion. In addition, some data were reported on the final combustion products of Al particles, mostly in the form of Al oxide residue [2]. However, detailed studies on the initial stage of Al oxide formation, which involves nucleation, particle growth due to "chemical conden-

* Corresponding author. Fax: +7-3832-342350.
E-mail address: onischuk@ns.kinetic.nsc.ru (A.A. Onischuk).

0010-2180/$ – see front matter
doi:10.1016/j.combustflame.2004.04.001

sation," coagulation followed by coalescence, and aggregate formation, have not yet been performed.

The investigation of the peculiarities of the above processes may improve our understanding of metalized solid propellant combustion [3]. It is known that Al_2O_3 particles ("smoke") play and important role in the performance of solid motors [4]. They cause two-phase losses of specific impulse (negative effect on the total energetics of the motor) and provide damping for the acoustic oscillations in the combustion chamber (positive effect on combustion stability). Actually, the combustion of Al in a solid motor proceeds at elevated pressures in the presence of CO_2, CO, and H_2O. Therefore, direct application of the data obtained in experiments in air at atmospheric pressure could not be done for solid motor combustion conditions. Nevertheless, the knowledge of more simple mechanism details may give insight into the processes occurring in real systems.

It is worthwhile to note that at the present time the problem of disposal of solid motors, that are out of military service becomes actual. One of the simplest methods of disposal is open firing of the motor with the nozzle removed. In this case a large number of unburned Al droplets continue burning in the air, forming oxide aerosols propagating in the atmosphere. The properties of such aerosol particles have an important meaning in estimation of their environmental impact. In particular, due to high specific surface the fine aerosol particles are able to accumulate and transport some harmful combustion products [5] of the motor incineration. Therefore, to estimate possible environmental impact it is necessary to know the mechanism of fine Al oxide particle formation and the characteristics of particles.

In the current research, the burning Al droplets were generated by combustion of small samples of solid propellant in air. Our previous work [6] showed that the fine Al oxide particles formed in this combustion process are aggregates of charged primary particles. The goal of the present work was detailed investigation of the mechanism of charged alumina aggregate formation. To this end we studied temporal behavior of the aggregate size, morphology, and charge. The role of Coulomb interactions in coagulation of aggregates was also investigated. Numerical simulation was carried out in order to estimate the role of different mechanisms in the particle-charging process.

2. Experimental

Formation of Al_2O_3 aggregates was studied in combustion in air of small ($1 \times 1.5 \times 20$ mm^3) samples of solid rocket propellant containing aluminum of size 5–15 μm, ammonium perchlorate of size 200–400 μm, and binder (see Fig. 1). The mass of aluminum in one sample was about 6 mg.

Fig. 2 shows the experimental setup. A sample of solid rocket propellant was burned in a combustion chamber of 20 litres volume filled before the experiment with filtered air. In filtering, a high-efficiency Petrianov aerosol filter [7] was used. Air pressure in the vessel was 1 atm. The sample combustion time was about 5 s. The combustion of the sample was accompanied by ejection of burning agglomerates, which were actually liquid aluminum droplets 100–500 μm in diameter. In fact, solid propellant combustion in our experiments was just an easy way to

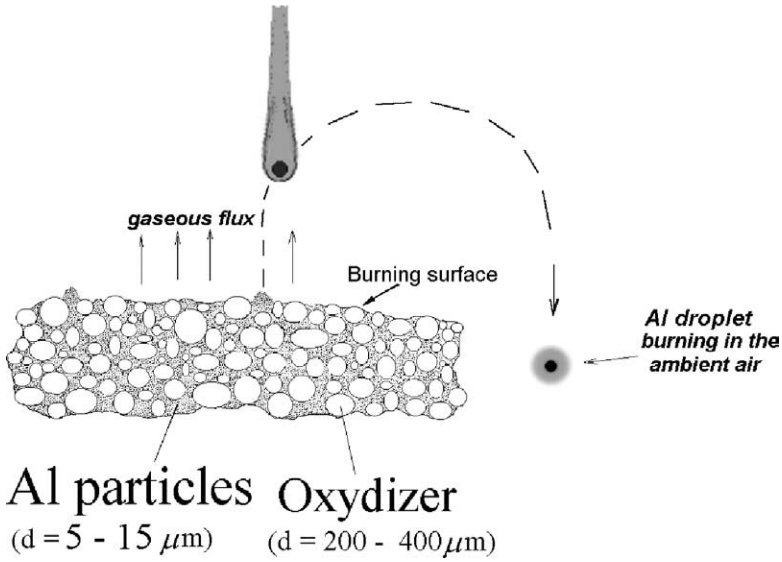

Fig. 1. Structure of the solid propellant specimen and schematic view of the Al droplet burning in ambient air.

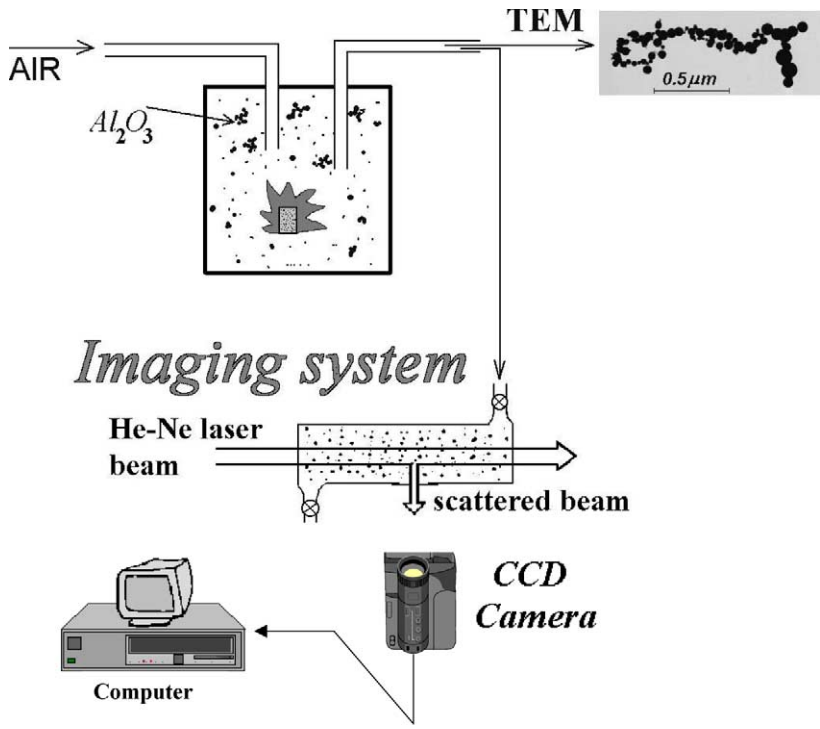

Fig. 2. Schematic diagram of experimental setup. The electron diffraction micrograph and a typical image of a Al_2O_3 aggregate are given in the inserts.

produce burning aluminum droplets. These droplets moved downward in the ambient air and generated Al_2O_3 aerosol (Fig. 1). From the video records we determined the droplet combustion time as 0.1–0.5 s and the droplet velocity as about 30–150 cm/s.

The Al_2O_3 aerosol was left in the vessel for a certain time (from 1 to 20 min after the propellant sample combustion finished). Then the alumina aerosol was sucked from the combustion chamber and sampled thermophoretically for transmission electron microscopy (TEM) JEM-100SX analysis. TEM analysis gave information about the size and morphology of aerosol particles.

The original video system was used to observe the coagulation of alumina aggregates [8,9]. In these experiments a probe of aerosol was sucked from the combustion chamber. Then the probe was injected into an optically accessible cell elaborated by Fuchs and Petrianov [10]. A focused He–Ne laser beam passed through the cell volume. A light scattered by aerosol particles at an angle of 90° passed through a flat window to a microscope objective and then to a CCD camera connected to the video system. The objective draws an image of particles located in the illuminated volume of the cell on the light-sensitive CCD matrix with 15× magnification. The visualization field in the optical cell is nearly 300 × 400 μm. The focal depth in the object space is about 30 μm. The spatial resolution of the system is nearly 3 μm, which allows obtaining resolved images of aggregates larger than 3 μm. For smaller sizes, the aggregates are visible as spots.

To create the homogeneous electric field two parallel flat electrodes were installed in the cell. The distance between electrodes was 0.25 cm. The movement of the aggregates in the electric field gave information on the electric charge and dipole moment of resolved visible aggregates.

Additional observations of the burning surface of the propellant sample and burning aluminum particles were carried out using high-speed photography [11]. The zone above the propellant burning surface was backlight illuminated by the intense short pulses (1 μs) of the Xe-lamp. The transmitted light formed a shadow image of the zone adjoining the burning surface by means of an objective. The range of 400–500 nm was selected by a bandpass filter in the transmitted light. The self-radiation of the flame is low in this spectral range, therefore the burning surface and detached droplets were detected clearly enough (Fig. 3a).

3. Results

Fig. 3a presents two consecutive shadow frames illustrating the burning processes at the surface of the

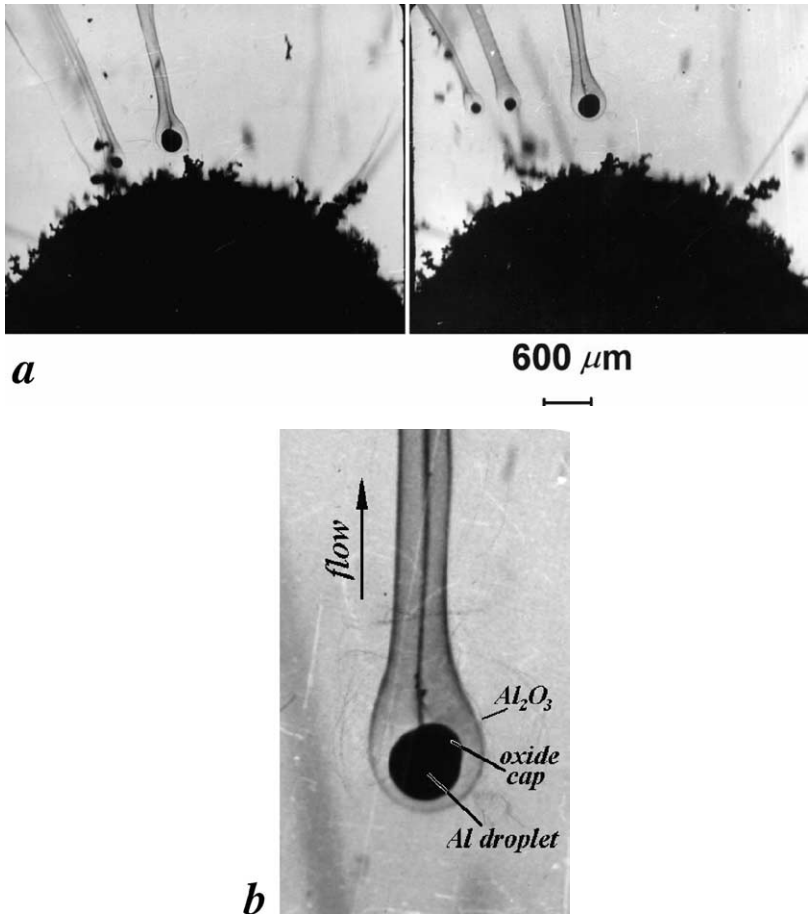

Fig. 3. High-speed photographic data, 2000 frames per second: (a) two consecutive shadow images illustrating generation of agglomerates by the propellant burning surface; (b) magnified showing the Al droplet, oxide cap, and Al_2O_3 tail.

solid propellant. The propellant under study follows the strong agglomeration scenario [12–14]. In this scenario, melting and ignition of aluminum particles occur mostly at the burning surface. They form relatively coarse round agglomerates that start burning within the propellant surface layer with the formation of a typical halo and smoke tail.

In the experiments performed in the present work, the burning agglomerates ejected from the propellant surface move in the ambient air. Fig. 3b presents a magnified view of the burning aluminum agglomerate. One can see the alumina smoke tail and Al oxide cap on the surface of the droplet.

Examination of TEM images showed that Al_2O_3 aerosol consists of chainlike aggregates (Fig. 4) composed of small spherical primary particles. The size of the primary particles is in the range 10–150 nm. The radius of the aggregates was determined from TEM micrographs as

$$R = \frac{1}{2}\sqrt{LW}, \tag{1}$$

where L and W are the dimensions of the rectangle enclosing the image of a single aggregate [15]. Fig. 5 presents the arithmetic mean radius R of aggregates vs. coagulation time, defined as the time elapsed since the specimen combustion was finished up to the sampling moment. Fig. 6 shows an example of the frequency distribution of the Al_2O_3 aggregate radius R after a coagulation time of 1 min. This distribution can be fitted by the lognormal function with standard geometric deviation $\sigma_g = 2.1$.

The aggregate morphology was described in terms of a fractal-like dimension D_f, which was determined from a power relationship between the aggregate mass M and radius R measured by TEM analysis [16]:

$$M \propto R^{D_f}. \tag{2}$$

To determine D_f the values of aggregate masses were plotted as $\log M$ vs. $\log R$. Two approaches to aggregate mass determination from the TEM data have been employed. The first approach is based on the

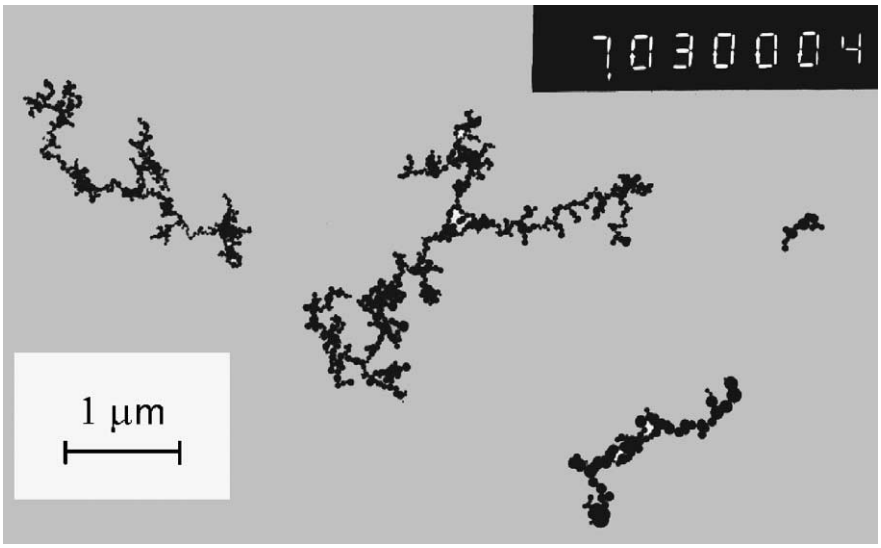

Fig. 4. TEM images of Al_2O_3 aggregates sampled after coagulation times 5.5 min.

densitometric processing of the aggregate TEM images. To determine the aggregate mass (in arbitrary units) we measured the "integral optical density" of an individual aggregate TEM image. It was assumed that the local optical density in the aggregate image is proportional to the local aggregate thickness. Thus, the total aggregate mass is proportional to the integral optical density. This approach seems to be reasonable because it is known that even the fractal-like dimension of two-dimensional projection is approximately equal to the D_f of the original 3D object if $D_f < 2$ [16,17]. The second approach involves measurement of the diameter of each primary particle composing the aggregate followed by direct calculation of the total aggregate mass (using the value 3.96 g/cm^3 for density of alumina). Both approaches gave the same fractal-like dimension $D_f = 1.60 \pm 0.04$. It was determined that the fractal-like dimension did not change with coagulation time in the range 1–20 min. Fig. 7 shows aggregate mass M vs. radius R in logarithmic coordinates and includes all data corresponding to different coagulation times in the range 1–20 min.

By examining the aggregates, one can determine the average diameter d_{ag} of primary particles for selected aggregate. It was revealed that the d_{ag} value differs from aggregate to aggregate. To demonstrate the difference in d_{ag} for various aggregates, Fig. 8 presents mass distribution functions of primary particles for two different aggregates. The essential difference between these two functions is seen. In particular, the mean arithmetic diameter differs twice for these two aggregates (see the caption to Fig. 8). Fig. 9 shows the frequency distribution of d_{ag}. The demonstrated variation of d_{ag} for the aggregates is probably

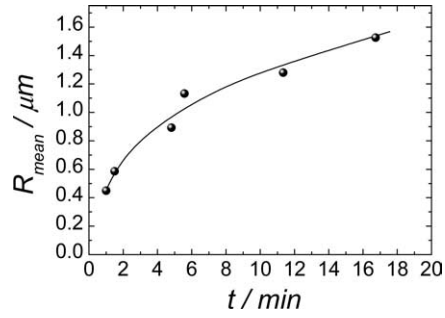

Fig. 5. Arithmetic mean radius of aggregates vs. coagulation time (TEM data).

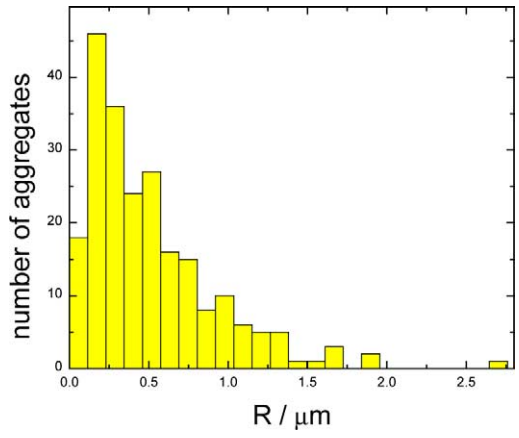

Fig. 6. Frequency distribution of aggregate radius R determined from TEM measurements. Coagulation time 1 min. Arithmetic mean radius for this distribution $R_{mean} = 0.45 \pm 0.03$ μm.

caused by the difference in the burning conditions (local vapor concentration, temperature distribution, and size of flame zone) around different aluminum droplets. Fig. 10 shows the image of the real aggregate. One can see that this aggregate consists of several groups of primary particles, which differ from each other considerably by the diameter of primary particles. We call these groups primary clusters. One may assume that the primary clusters originated in the combustion of different aluminum droplets and later formed the final aggregate due to coagulation.

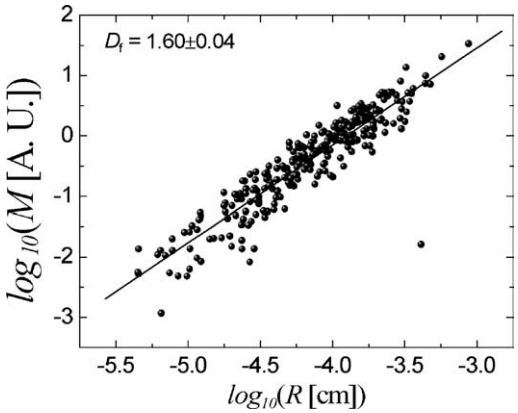

Fig. 7. M vs. R plots of TEM data for Al_2O_3 aggregates. M is the aggregate mass determined by the densitometric elaboration of TEM images; $R = \frac{1}{2}\sqrt{LW}$, where L and W are the dimensions of the rectangle enclosing the images of a single aggregate. The solid line corresponds to the relationship $M \propto R^{D_f}$, where $D_f = 1.6$.

We estimated the average number N_p of primary particles in clusters and the average cluster radius R_{clust} as follows: $N_p \approx 270$ and $R_{\text{clust}} \approx 0.5$ μm. One can compare the value of the primary cluster radius with the radius of aggregates R presented in Fig. 5 as a function of time. It is evident from this comparison that at the initial stage of coagulation ($t \approx 1$ min) only primary clusters are presented in the gas phase. Later, the aggregates composed of few primary clusters are formed.

Movement of alumina aggregates in a homogeneous electric field with an intensity of 200 V/cm organized within the optical cell has been studied using the video system. Fig. 11 gives an example of the movement of two aggregates in an electric field. One can see that one aggregate moves downwards (negative charge), while the second aggregate moves upwards (positive charge). We estimated the aggregate net charge from the balance between the Coulomb force and the drag force F_D,

$$n_{\text{ch}} eE = F_D, \tag{3}$$

where n_{ch} is the number of elementary charges in the aggregate, e is the elementary charge (4.8×10^{-10} units of CGSE), and E is the electric field intensity. The drag force is [18]

$$F_D = \frac{6\pi \upsilon \eta R_m}{(1 + \lambda A / R_m)}, \tag{4}$$

where η is the viscosity coefficient for air, υ is the aggregate velocity, R_m is the mobility equivalent radius, λ is the gas mean free path, and A is the Cunningham

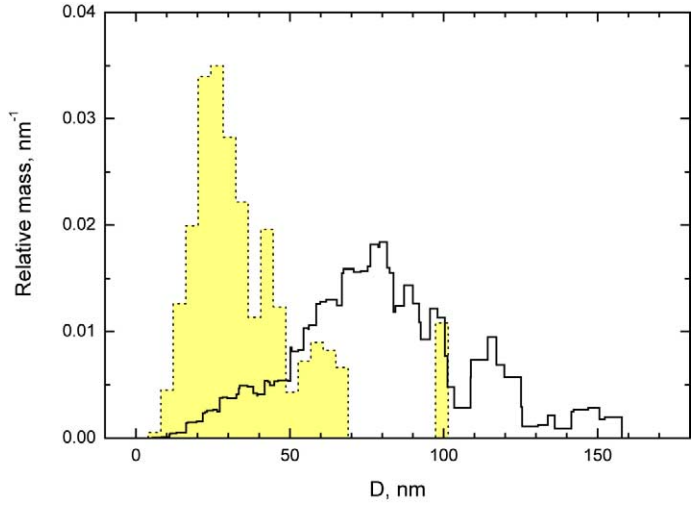

Fig. 8. Mass distribution of primary particles over diameter in two aggregates selected as examples. A separate bar at 100 nm correspond to one coarse particle presented in aggregate. The dotted line histogram involves 1955 primary particles; the arithmetic mean diameter for these primary particles is 18 nm, and the standard error of the mean diameter is 0.2 nm. The solid line histogram involves 2847 primary particles; the arithmetic mean diameter for these primary particles is 35 nm, and the standard error of mean diameter is 0.8 nm.

correction factor ($A = 1.26$). In estimating the charge of the aggregate with Eqs. (3) and (4) the crucial point was determination of R_m. Two different approaches were used.

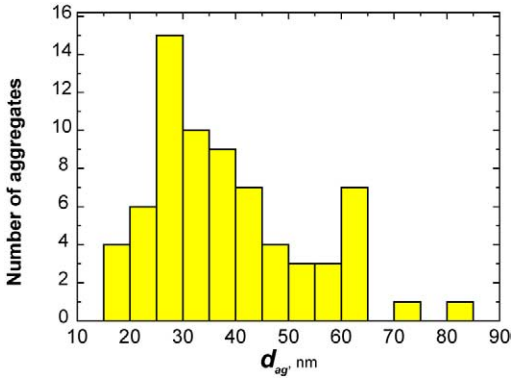

Fig. 9. Frequency distribution of mean primary particle diameter d_{ag} determined for an ensemble of 70 aggregates.

In the first approach, the mobility equivalent radius of each aggregate was derived from the observation of its Brownian motion without an electric field. An example of the aggregate trajectory observed by the video system is presented in Fig. 12. The aggregate diffusion coefficient D was determined from the Einstein equation,

$$\overline{(\Delta x)^2} = 2Dt, \tag{5}$$

$$\overline{(\Delta x)^2} = \frac{\Delta x_1^2 + \Delta x_2^2 + \cdots + \Delta x_N^2}{N},$$

where $\Delta x_1, \Delta x_2, \ldots, \Delta x_N$ are successive displacements of the aggregate along horizontal x-axis over time interval t (see Fig. 12). Then the effective radius was derived from the expression for diffusion coeffi-

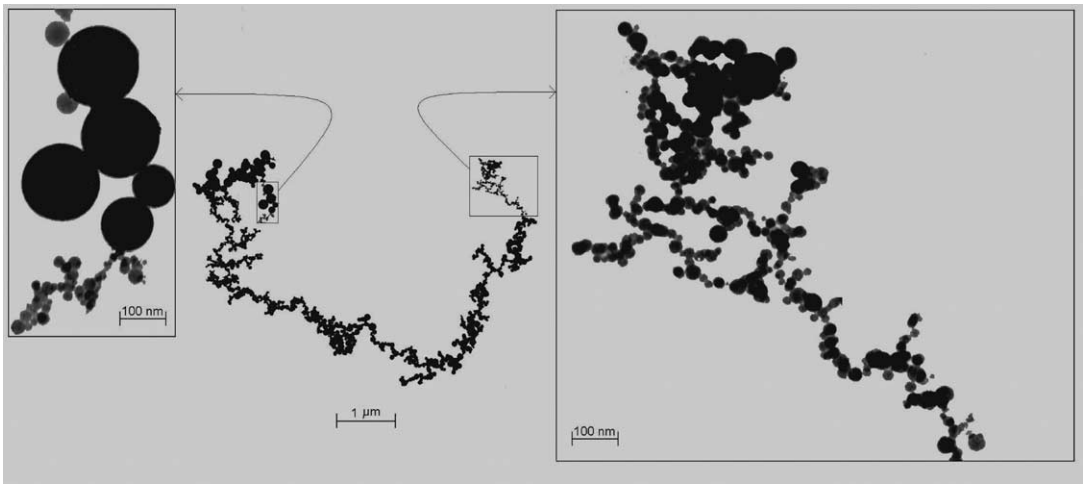

Fig. 10. TEM image of Al_2O_3 aggregate.

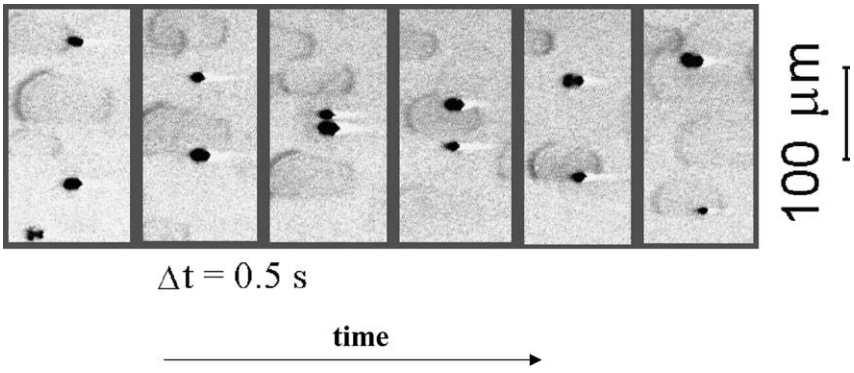

Fig. 11. Series of flames illustrating the movement of aggregates in a homogeneous electric field, 200 V/cm. The field is directed vertically. (In the last two frames the upper aggregate looks split and the lower aggregate diminishes in size. In fact there is no splitting or decrease in size. These apparent effects are caused by the rotation of complex shape aggregates.)

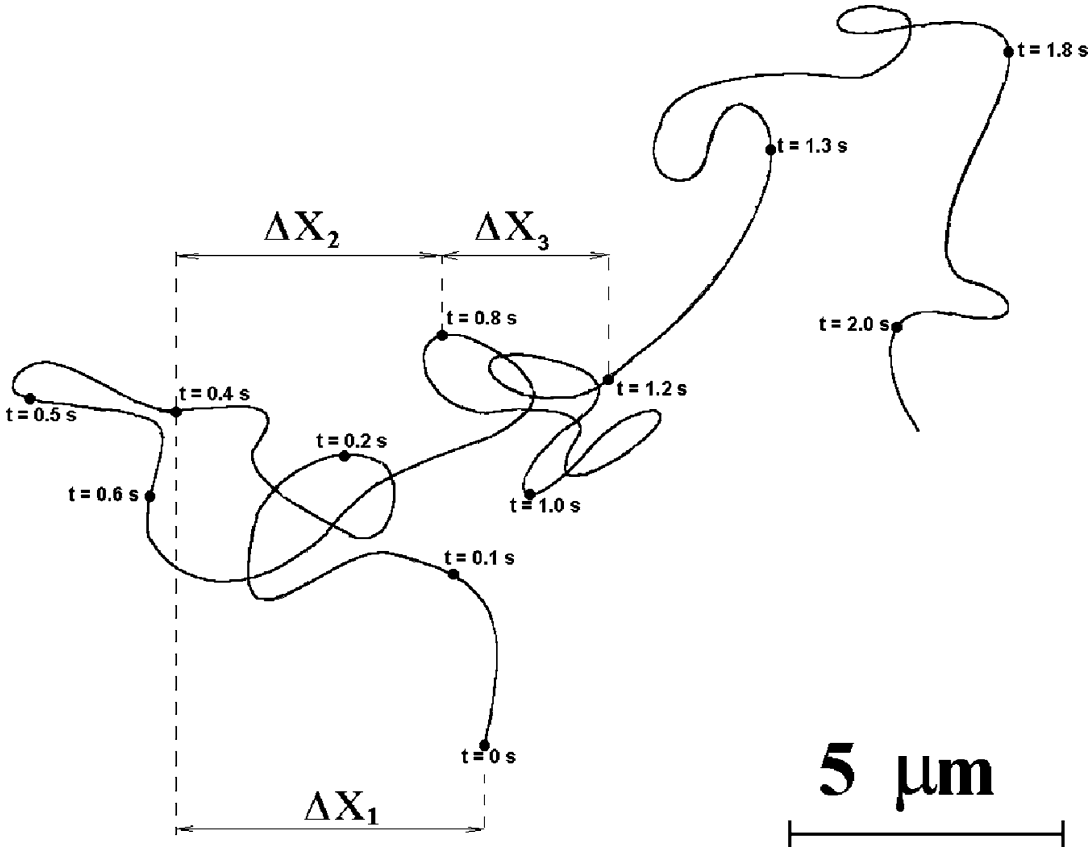

Fig. 12. Example of the aggregate trajectory registered by the video system.

cient [19],

$$D = \frac{kT(1+\lambda A/R_m)}{6\pi R_m \eta}, \tag{6}$$

where k is the Boltzmann constant, T is the temperature. In our measurements the time interval was chosen as $t = 0.4$ s; the number of readings was $N \geqslant 25$. In this case the video data processing resulted in an error of R_m less than 30%.

After examination of the aggregate Brownian motion the electric field was switched on to measure the velocity of aggregate movement due to electric force. This approach resulted in the charge distribution over aggregates presented in Fig. 13a.

In the second approach, the same average mobility radius was used to characterize each aggregate recorded by the video system. This average R_m was determined by processing the TEM images assuming equivalence of the mean mobility radius R_m and mean projected area radius R_a [20]. Fig. 13b shows a plot of the frequency distribution of aggregate charge for this method of experimental data treatment. It represents a symmetric bipolar charge distribution of aggregates. The typical aggregate net charge is about 10 elementary units. Both histograms presented in Figs. 13a and 13b were fitted by the Gaussian function

$$G(n_{\mathrm{ch}}) = \frac{P}{w\sqrt{\pi/2}} \exp\left(-\frac{2n_{\mathrm{ch}}^2}{w^2}\right), \tag{7}$$

where n_{ch} is the number of elementary charges per aggregate, w is the parameter characterizing the width of the distribution, and P is a fitting parameter to adjust number of aggregates. The fitting procedure gives $w = 12.0 \pm 1.0$ and 12.7 ± 0.4 for histograms a and b, respectively. Thus, one can see reasonably good agreement between two histograms that indicates the validity of both methods of aggregate charge distribution measurement.

Another important experimental finding is that some aggregates are dipoles. This is demonstrated by their rotation when the electric field polarity is changed (Fig. 14).

To understand how significant the role of the Coulomb interactions in the coagulation process is we examined the sticking of free aggregates to the tendrils, which constitutes the Al_2O_3 deposit on the surface. The experiment was carried out as follows.

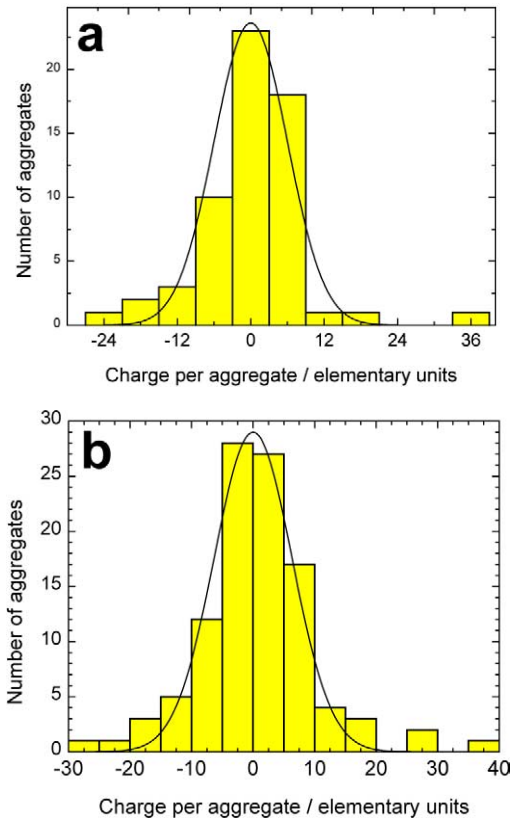

Fig. 13. Frequency distribution of aggregate charge determined by the video system. Coagulation times is 4 min; (a) the equivalent mobility radius R_m for each aggregate considered was determined from the Brownian motion observation using Eq. (6); (b) the same average mobility radius was used for each aggregate to estimate the net charge. The average R_m was determined from TEM images, assuming that it is equal to the average projected area radius (see text). The solid lines are governed by the Gaussian function $G(n_{\mathrm{ch}}) = \frac{P}{w\sqrt{\pi/2}} \exp(-2n_{\mathrm{ch}}^2/w^2)$, where n_{ch} in the number of elementary charges per aggregate, w is the parameter, which characterize the width of the distribution, P is a fitting parameter to adjust number of aggregates. The fitting procedure gives $w = 12.0 \pm 1.0$ and 12.7 ± 0.4 for histograms a and b, respectively.

A fine glass filament of diameter 300 μm was fixed inside the optical cell. The objective of the visualizing system was focused at the surface of this filament. Then the alumina aerosol was injected into the cell. A few minutes after the aerosol injection we observed tendrils growing on the filament surface due to continuous aggregate sticking. The process of aggregate sticking to the tendrils is illustrated in Fig. 15. The series of aggregate images was recorded with the time interval 0.04 s. The nonlinear aggregate trajectory is the evidence of attractive Coulomb interaction between the aggregate and the tendril.

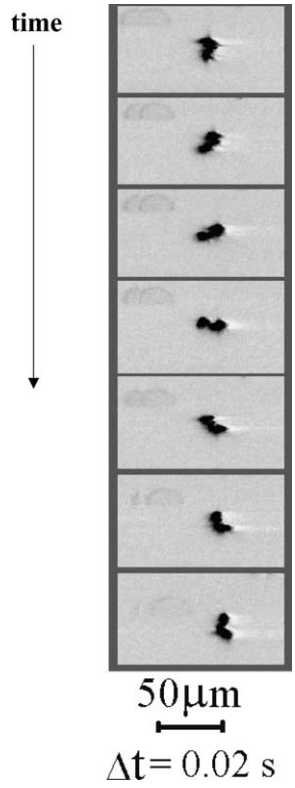

Fig. 14. Series of images illustrating the aggregate rotation after the switching of the electric field polarity. The electric field is directed vertically. The frames are separated by a time interval $\Delta t = 0.02$ s (shown in the figure).

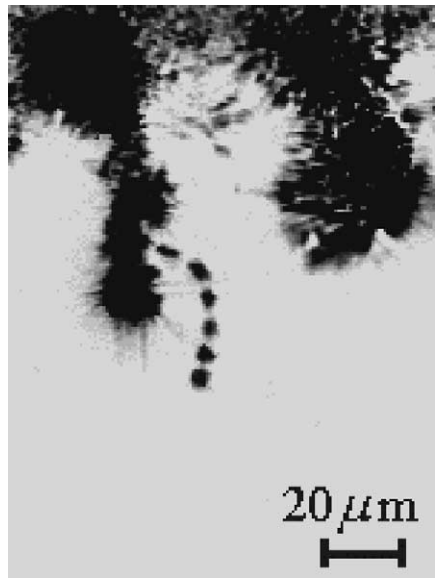

Fig. 15. Video recording illustrating consecutive stages of aggregate–tendril collision. Time interval between stages $\Delta t = 0.04$ s.

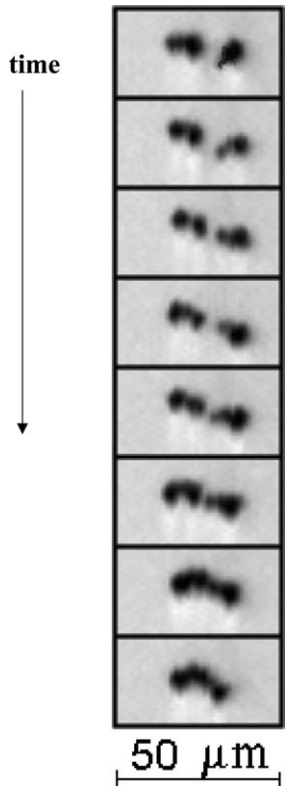

Fig. 16. Aggregate–aggregate collision process without external electric field. Time interval between consecutive frames is 0.04 s.

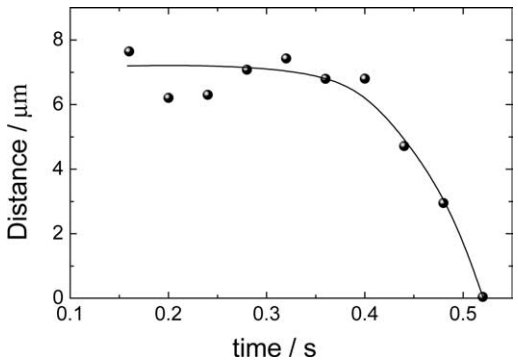

Fig. 17. Distance vs. time between the aggregates presented in Fig. 16.

Fig. 16 demonstrates results of direct observation of aggregate–aggregate collision accompanied by the Coulomb interaction. In Fig. 17, the distance between these aggregates vs. time is plotted. One can see that the velocity of mutual approach increases with time and reaches a maximum value at the moment of collision that indicates an essential influence of the Coulomb interaction on the coagulation process.

4. Discussion

4.1. Aggregate dipole moment

Let us estimate the dipole moment of the aggregate pictured in Fig. 14. The aggregate rotation due to the moment of external force is governed by the equation [19]

$$d\theta/dt = B_\omega M_\theta, \tag{8}$$

where θ is the rotation angle, B_ω is the "rotational mobility," M_θ is the moment of external force. To evaluate the dipole moment, the aggregate shown in Fig. 14 was considered as an ellipsoid with the ratio of the long axis to the short one equal to $\beta = 6$. The "rotational mobility" is a function of β. For $\beta = 6$ one has [19]

$$B_\omega = 5.9\left(\pi\eta L^3\right)^{-1} \text{ (CGSE units)}, \tag{9}$$

where L is the length of aggregate ($L \approx 15$ μm) and η is the air viscosity equal to $\eta = 1.83 \times 10^{-4}$ Poise at room temperature. Thus, from the values of $d\theta/dt \sim 30$ s^{-1} (see Fig. 14) we can estimate the moment of force M_θ by using Eqs. (8) and (9) as $M_\theta \sim 10^{-11}$ [dyn cm]. To have a rough idea about the possible charge distribution in this aggregate we assume that positive $+q$ and negative $-q$ charges are localized at the opposite ends of the aggregate. As a result, from the value of M_θ we estimate $q \approx M_\theta/L$, which gives $q \approx 15$ elementary units.

4.2. Fractal-like dimension

It was found that the fractal-like (or Hausdorf) dimension of alumina aggregates is about $D_f \approx 1.6$ (Fig. 7). In general, the value of D_f depends on the mechanism of aggregate formation. The mechanism of diffusion-limited cluster–cluster aggregation (DLCCA) results in $D_f \approx 1.8$ [16]. The DLCCA mechanism assumes that aggregates approach each other due to the Brownian diffusion and there are no long-range interactions between colliding aggregates. On the other hand, long-range attractive interaction between coagulating particles or aggregates results in a smaller value of fractal-like dimension [21–23]. Thus, we can explain experimentally determined relatively low fractal dimension by Coulomb interactions between colliding aggregates.

4.3. Possible mechanisms of Al_2O_3 nanoparticle formation and aggregation under combustion of aluminum droplets

As a rule, aluminum droplets ignite at a temperature near to or higher than the melting point of

Al_2O_3 (2323 K) [24]. After the ignition the particle is rapidly self-heated up to the aluminum boiling point, 2730 K. The molten aluminum can dissolve up to about 0.1 at. % of oxygen [25]. The solution boiling temperature decreases with the increasing concentration of dissolved oxygen from 2730 K (pure aluminum) to 2510 K (saturated oxygen solution). Thus, the temperature of the burning Al droplet can be considered equal to about 2500 K. The temperature in the flame zone is about 3200 K [26].

Aluminum burns in the vapor phase because of the lower boiling point compared with the final combustion product Al_2O_3. The reaction is believed to be limited by the diffusion of oxidizer towards the droplet and the outward flux of gaseous aluminum. The reaction (or flame) zone at pressure of 1 atm is located in the region $r/r_0 = 3$–6 [24], where r and r_0 are the radial coordinate and droplet radius, respectively. In the flame zone a homogeneous reaction takes place between the gaseous aluminum and oxidizer (oxygen in ambient atmosphere). The oxidized products consist of gaseous suboxides such as AlO, AlO_2, Al_2O, Al_2O_2. These oxidized products condense in the flame zone to form Al_2O_3 smoke. The condensation in aluminum combustion is different from the classical nucleation theory. In aluminum combustion the condensation proceeds via heterogeneous chemical reactions at the surface of alumina nanoparticle. The chemical condensation reactions discussed in the literature are [27]

$$2Al + \frac{3}{2}O_2 \rightarrow Al_2O_3\,(l), \tag{10}$$

$$2AlO + \frac{1}{2}O_2 \rightarrow Al_2O_3\,(l), \tag{11}$$

$$AlO_2 + AlO \leftrightarrow Al_2O_3\,(l), \tag{12}$$

$$Al_2O + O_2 \rightarrow Al_2O_3\,(l), \tag{13}$$

$$Al_2O_2 + \frac{1}{2}O_2 \rightarrow Al_2O_3\,(l), \tag{14}$$

$$AlO_2 + AlO_2 \rightarrow Al_2O_3\,(l) + \frac{1}{2}O_2. \tag{15}$$

The Al_2O_3 particle growth is characterized by simultaneous coagulation and coalescence. The resulting nanoparticles are liquid and spherical in the reaction zone. In our experiments the burning aluminum droplets were falling down in the ambient air, creating a tail composed of Al_2O_3 nanoparticles (see Fig. 18). The droplet velocity is about 100 cm/s. This value is too slow to affect considerably the temperature distribution in the reaction zone [24,27]. At the distance from the droplet surface of several radii the temperature decreases to the Al_2O_3 melting point [24] (Fig. 18). Here and downstream the coagulation process results in formation of aggregates composed of spherical primary particles (Fig. 4). The

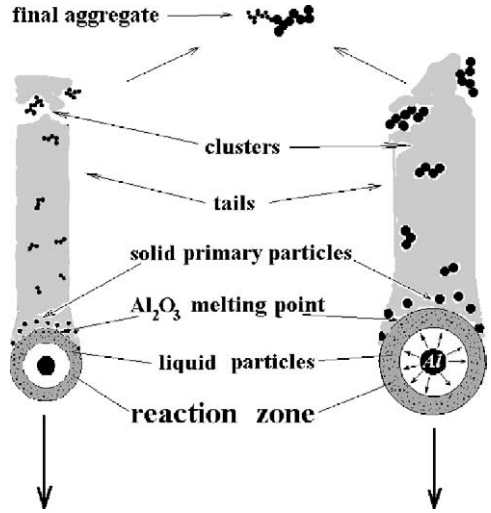

Fig. 18. Scheme pf the Al_2O_3 coagulation process.

particle concentration n_s in the periphery of the reaction zone where the solidification occurs can be easily estimated from the rate w_{Al} of aluminum evaporation from the droplet, droplet velocity, and mean diameter of primary alumina particles, which is about 40 nm (Fig. 9). The rate w_{Al} can be roughly estimated from the droplet burning time. For calculations we have taken the droplet burning time of 0.2 s (which corresponds to a diameter of 200 μm). Thus, we have $w_{Al} \approx 1.3 \times 10^{18}$ atoms per second and the particle concentration

$$n_s \approx 3 \times 10^{11}\ \mathrm{cm}^{-3}. \tag{16}$$

It was shown above that the aggregates sampled from the reaction chamber consist of primary clusters. The diameter of primary particles in the same cluster varies to a small extent, while the diameter of particles from different clusters can differ considerably (see, for example, Fig. 10). Thus, we can assume that different primary clusters arise from different smoke tails, i.e., from different burning droplets. We can estimate the average cluster formation time τ_{clust} by using the average number of primary particles in a cluster ($N_p = 270$) as a basic parameter. In other words, the whole aggregate formation process can be divided into two stages—cluster formation from primary particles of the same smoke tail and final aggregate formation from clusters originated from different tails. The value τ_{clust} is a characteristic time of the first stage of the process.

Using the particle concentration $n_s \approx 3 \times 10^{11}$ cm^{-3} (see Eq. (16)) at the moment of alumina particle solidification we can estimate the cluster concentration n_{clust} at the time τ_{clust} as

$$n_{clust} \approx \frac{n_s}{N_p} \times \frac{T_{melt}}{T_{room}} \approx 10^{10}\ \mathrm{cm}^{-3}. \tag{17}$$

Here T_{melt} and T_{room} are the melting temperature for alumina and the room temperature, respectively. When estimating n_{clust} in Eq. (17), we assume that the temperature is close to the room temperature at the end of the primary cluster formation stage.

The rate of aggregate concentration decrease due to coagulation could be approximately described by the second-order kinetics

$$\frac{dn}{dt} = -Kn^2, \tag{18}$$

where n is the cluster concentration and K is the cluster coagulation constant. For clusters with the mobility equivalent radius R_m the coagulation constant is calculated by

$$K \approx 8\pi D R_m, \tag{19}$$

where D is the diffusion coefficient (see Eq. (6)). The time of the cluster growth is determined by the late stages of the cluster coagulation process when the radius R (Eq. (1)) is equal to the primary cluster geometric radius in final aggregates $R_{clust} = 0.5$ μm (see the section *Results*). It is easy to estimate the equivalent mobility radius from R_{clust} [8,15,19], which is approximately equal to $R_m \approx 0.3$ μm. Thus, for $T = 295$ K we have $D = 5 \times 10^{-7}$ cm^2/s. From (18) and (19) we obtain the cluster growth time,

$$\tau_{clust} \approx \frac{1}{K n_{clust}} \approx 0.2 \text{ s}. \tag{20}$$

Thus, we can conclude that at time $t < \tau_{clust}$ the coagulation of particles originating from the same droplet occurs, resulting in cluster formation; at $t > \tau_{clust}$ the coagulation of clusters originating from different Al droplets occurs, resulting in final aggregate formation from different clusters.

4.4. Possible routes for charged particle formation

The experimental data presented in Figs. 11 and 13–17 demonstrate that the alumina aggregates formed in aluminum droplet combustion are charged. Both positively and negatively charged aggregates are present. The typical charge is about a few elementary units.

One of the possible mechanisms for charged particle formation is the thermal emission of electrons from the boiling droplet of aluminum. The electron current from the surface of aluminum is determined by the Richardson–Dushman formula for electron emission,

$$j_e = AT^2 \exp\left(-\frac{W_0}{kT}\right), \tag{21}$$

where j_e is the electron current density from the heated surface, A is a factor equal to 60–100 A/(cm^2 K^2) for pure metals, W_0 is the work function (equal to 4.25 eV for aluminum), k is the Boltzmann constant, and T is the temperature. Under steady state conditions the electron density around the aluminum droplet is governed by the Poisson equation,

$$\Delta\varphi = -4\pi\rho, \tag{22}$$

where φ is the electric potential and ρ is the volume charge density. The Boltzmann equation for the volume charge density is

$$\rho = C \exp\left(-\frac{e\varphi}{kT}\right). \tag{23}$$

Here C is a coefficient which can be calculated from the boundary conditions,

$$C = \rho_0 \exp\left(\frac{e\varphi_0}{kT}\right), \tag{24}$$

where ρ_0 is the volume charge density near the surface of the droplet, e is the elementary charge, and φ_0 is the electric potential at the surface of the droplet. The ρ_0 value can be estimated from the balance between the emission current j_e and the current of electrons j_{back} coming back from the gas phase to the surface. The electron current j_{back} coming to the unit surface area of the droplet is

$$j_{back} = \frac{n_e v_e}{4}, \tag{25}$$

where n_e is the electron concentration in the gas phase near the surface ($n_e = \rho_0/e$) and v_e is the thermal velocity of electrons in the gas phase,

$$v_e = \sqrt{\frac{8kT}{\pi m_e}} \tag{26}$$

(m_e is the electron mass). To calculate the electron concentration in the gas phase around the Al droplet as a function of the radial coordinate r we set the temperature profile $T(r)$ in accordance with the literature data [24] (see Fig. 19). Eqs. (22) and (23) were solved together numerically. The boundary conditions for electric potential φ were

$$\varphi|_{r=r_0} = 0, \tag{27}$$

$$\varphi|_{r=\infty} = \frac{q}{r_0} - \int \frac{\rho(r)}{r}\, dV, \tag{28}$$

where r_0 is the droplet radius, q is the net droplet charge, and $\rho(r)$ is the charge density in the space around the droplet. The second term in Eq. (28) is a volume integral over the space around droplet. In addition, the neutrality condition

$$q = \int \rho(r)\, dV, \tag{29}$$

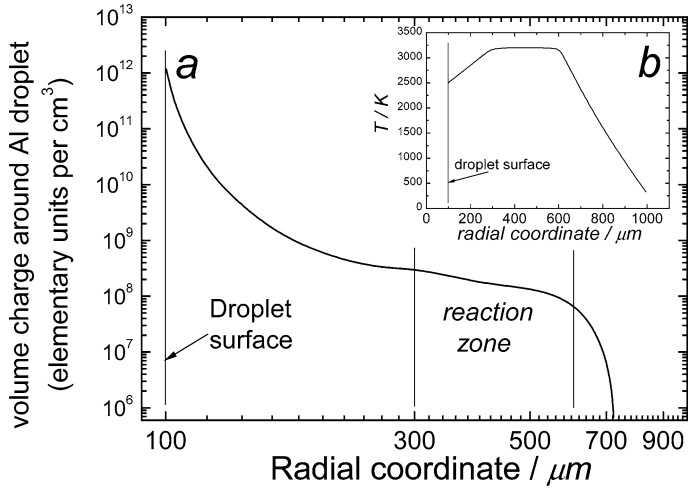

Fig. 19. (a) Calculated radial distribution of volume change around burning Al droplet. The temperature profile was set according to [26] as shown in insertion (b).

where the right hand term is a volume integral over the space around the droplet, was used.

One of the results of this calculation is the value of the positive net charge q of the aluminum droplet ($q = 8 \times 10^5$ elementary charges). Another result is the volume charge concentration in the gas phase around the droplet as a function of the radial coordinate r. Fig. 19 demonstrates that the thermal emission of electrons results in the volume charge in the reaction zone of about 10^8–10^9 elementary units per cm^3. The electron concentration near the droplet surface is about 10^{12} cm^{-3}.

The relatively high electron concentration near the droplet surface can result in formation of negative ions Al^- via the reaction

$$e^- + Al \leftrightarrow Al^-. \tag{30}$$

The equilibrium constant can be written as

$$K_0 = \frac{[e^-][Al]}{[Al^-]} = \frac{Z_e g^0}{g^-} \exp\left(-\frac{\varepsilon}{kT}\right), \tag{31}$$

where $Z_e = 2(2\pi m_e kT/h^2)^{3/2}$ is the partition function for the electron, g^0 and g^- are the degenerations for Al and Al^-, equal to 6 and 9, respectively, ε is the electron affinity for aluminum, equal to 0.44 eV, k is the Boltzmann constant, T is the temperature, m_e is the mass of the electron, and h is the Planck constant. At $T = 2500$ K the equilibrium constant is $K_0 = 5.2 \times 10^{19}$ cm^{-3}, the concentration of aluminum atoms near the boiling surface of droplet is $[Al] = 2.9 \times 10^{18}$ cm^{-3}. Thus, from (31), we obtain

$$\frac{[e^-]}{[Al^-]} \approx 18. \tag{32}$$

In other words, about 5% of the negative charges near the surface of aluminum droplet are presented in the form of Al^- ions.

It is also interesting to estimate the fraction of negative ions in the reaction zone. The most abundant intermediates in the reaction zone are Al, AlO, Al_2O, and AlO_2. Let us estimate as an example the ratio between the ions AlO_2^- and neutral molecules AlO_2. In the reaction zone the concentration of AlO_2 is $[AlO_2] \sim 10^{17}$ cm^{-3} [27]. The electron affinity for this species is 4.1 eV. From an equation similar to (31) we have the equilibrium constant $K_0 \sim 10^{14}$ cm^{-3}, which gives the ratio

$$\frac{[e^-]}{[AlO_2^-]} \sim 10^{-3}. \tag{33}$$

This estimate shows that the AlO_2^- ions will prevail over the electrons in the reaction zone.

One more possible reason for charged nanoparticle formation is the thermal emission of electrons from Al_2O_3 particles in the reaction zone. Zolotko et al. [28] estimated the charge of alumina nanoparticles formed due to combustion of aluminum particles in a laminar flame. The temperature of Al_2O_3 particles was taken as 3200 K. The typical size of alumina particles was assumed to be 70 nm. The net charge due to the thermal emission of electrons from Al_2O_3 particles was estimated to be equal to about 20 e.u. Thus, we can assume that in our case the thermal emission of electrons can result in a charge of alumina nanoparticles in the reaction zone of a few elementary units at least.

Finally, the mechanism of charged aggregate formation can be described as follows. A burning Al droplet falls down in the ambient air and has a posi-

tive net charge about 10^5–10^6 e.u. There is an electron cloud around the burning droplet. The electron concentration near the droplet surface is about 10^{12} cm^{-3}. The negative ion concentration in the reaction zone equals 10^8–10^9 cm^{-3} (Fig. 19). There are also Al_2O_3 particles in the reaction zone formed via reactions of chemical condensation. The positive charge of alumina particles is about a few e.u. These alumina nanoparticles are driven by a counterflow of air out of the reaction zone, producing a smoke tail. Both temperature and electron concentration are relatively low at the periphery of the reaction zone. Therefore, the net charge of the alumina particles also comes down when they leave the reaction zone. At the end, when the particles cool down to the room temperature, all neighboring electrons are caught by particles. Some particles are neutral. Some are positively charged because they did not succeed in catching enough electrons to neutralize the charge. Other particles are negatively charged because they caught an excess of electrons. Thus, there is a charge distribution over the primary particles. The coagulation of primary particles results in formation of charged primary clusters and, at the end, in formation of charged aggregates.

5. Conclusions

An experimental study of alumina nanoparticles formed by combustion of Al droplets in air was carried out. It was found that the alumina nanoparticles are generated as aggregates composed of primary particles. The diameter of primary particles is in the range 10–140 nm. The size of aggregates varies in the range from 0.1 to a few micrometers.

It was determined that the majority of the aggregates are charged either positively or negatively. The typical charge of aggregates is a few elementary units. Some of the aggregates are dipoles.

Microscopic real-time video registration showed that the charge of the aggregates affects considerably both the coagulation process and aggregate wall deposition.

The fractal-like dimension of the alumina aggregates has been determined as $D_f \approx 1.6$, which does not correspond to the diffusion-limited cluster–cluster aggregation model prediction. It was assumed that the Coulomb interactions between coagulating aggregates are responsible for this low value of the fractal-like dimension.

It was determined that the alumina aggregates consist of primary clusters. These clusters are composed of primary particles of approximately equal diameter. However, the mean diameter of the primary particles varies considerably for different clusters. The explanation follows from the fact that different clusters are formed by combustion of different aluminum droplets.

Calculations of the charge concentration around the burning droplet were carried out based on solution of Poisson–Boltzmann equations. It was determined that the electron concentration is about 10^{12} electron/cm^3 near the aluminum droplet surface, and in the reaction zone it equals 10^8–10^9 electron/cm^3. Estimations were made which demonstrated that close to the droplet surface about 5% of negative charges are represented by ions, while in the reaction zone the major part of negative charges are ions.

Acknowledgments

Financial support for this work was partially provided by the Presidium of the Russian Academy of Sciences (Project 8.17), Russian Foundation for Basic Research Projects 04-03-33163, and ISTC Project 2358.

References

[1] K.P. Brooks, M.W. Beckstead, J. Propulsion Power 11 (4) (1995) 769–780.
[2] A. Zenin, G. Kusnezov, V. Kolesnikov, Physics of Aluminum Particle Combustion at Zero-Gravity, AIAA Paper 99-0696, AIAA: Reston, VA, 1999, pp. 1–6.
[3] E.W. Price, R.K. Sigman, in: V. Yang, T.B. Brill, Wu-Zhen Ren (Eds.), Solid Propellant Chemistry, Combustion, and Motor Interior Ballistics, in: Progress in Astronautics and Aeronautics, vol. 185, AIAA, Reston, VA, 2000, pp. 663–687, P. Zarchan, Editor-in-Chief, Chapter 2.18.
[4] R.W. Hermsen, J. Spacecraft Rockets 18 (6) (1981) 483–490.
[5] D.P. Samsonov, V.P. Kiryukhin, N.P. Zhirikhina, R.I. Pervunina, J. Anal. Chem. 51 (11) (1996) 1218–1221, in Russian.
[6] V.V. Karasev, O.G. Glotov, A.M. Baklanov, A.A. Onischuk, V.E. Zarko, in: Proceedings of 33 International Annual Conference of ICT. Energetic Materials: Synthesis, Production and Application, Karlsruhe, Federal Republic of Germany, June 25–June 28, 2002, Report V14.
[7] A.A. Kirsch, I.B. Stechkina, N.A. Fuchs, J. Aerosol Sci. 5 (1975) 119–124.
[8] A.A. Onischuk, V.P. Strunin, V.V. Karasev, V.N. Panfilov, J. Aerosol Sci. 32 (2001) 87–105.
[9] A.A. Onischuk, S. di Stasio, V.V. Karasev, A.M. Baklanov, G.A. Makhov, A.L. Vlasenko, A.R. Sadykova, A.V. Shipovalov, V.N. Panfilov, J. Aerosol Sci. 34 (2003) 383–403.
[10] N.A. Fuchs, I.V. Petrianov, J. Phys. Chem. 4 (1933) 567–571.
[11] V.E. Zarko, V.V. Karasev, N.A. Silin, V.D. Gladun, L.Ya. Kashporov, in: Proceedings of the Eighth Interna-

tional Pyrotechnics Seminar, Chicago, 1982, pp. 728–735.
[12] E.W. Price, Combustion of Metalized Propellants, in: K.K. Kuo, M. Summerfield (Eds.), Fundamentals of Solid Propellant Combustion, in: Progress in Astronautics and Aeronautics, vol. 90, AIAA, New York, 1984, pp. 479–514, Chapter 14.
[13] O.G. Glotov, V.E. Zarko, V.V. Karasev, M.W. Beckstead, Condensed Combustion Products of Metallized Propellants of Variable Formulation, AIAA Paper 98-0449, 1998, pp. 1–7.
[14] O.G. Glotov, V.E. Zarko, Trans. Aeronaut. Astronaut. Soc. Rep. China 34 (3) (2002) 247–256.
[15] S.N. Rogak, U. Baltensperger, R.C. Flagan, Aerosol Sci. Technol. 14 (1991) 447–458.
[16] S.K. Friedlander, Smoke, Dust, and Haze, Oxford Univ. Press, New York/Oxford, 2000.
[17] R.J. Samson, G.W. Mulholland, J.W. Gentry, Langmuir 3 (1987) 272–281.
[18] P.C. Reist, Aerosol Science and Technology, McGraw–Hill, New York, 1993.
[19] N.A. Fuchs, The Mechanics of Aerosols, Pergamon, Oxford, 1964.
[20] S.N. Rogak, R.C. Flagan, H.V. Nguyen, Aerosol Sci. Technol. 18 (1993) 25–47.
[21] A.J. Hurd, W.L. Flower, J. Colloid Interface Sci. 122 (1988) 178–192.
[22] H.X. Zhang, C.M. Sorensen, E.R. Ramer, B.J. Olivier, J.F. Merklin, Langmuir 4 (1988) 867–871.
[23] R. Julien, P. Meakin, J. Colloid Interface Sci. 127 (1989) 265–272.
[24] T.P. Parr, D.M. Hanson-Parr, P. Bucher, R. Yetter, F. Dryer, in: Proceedings of the 32nd JANNAF Combustion Subcommittee Meeting, CPIA Publ. 631 (I) (1995) 409–417.
[25] Y.V. Levinsky, $P–T–x$ Binary Phase Diagrams of Metal Systems, Metallurgia, Moscow, 1990, in Russian.
[26] T.P. Parr, D.M. Hanson-Parr, in: V. Yang, T.B. Brill, W.-Z. Ren (Eds.), Solid Propellant Chemistry, Combustion, and Motor Interior Ballistics, in: Progress in Astronautics and Aeronautics, vol. 185, AIAA, Reston, VA, 2000, pp. 381–411, P. Zarchan, Editor-in-Chief, Chapter 2.5.
[27] P. Bucher, L. Ernst, F.L. Dryer, R.A. Yetter, T.P. Parr, D.M. Hanson-Parr, in: V. Yang, T.B. Brill, W.-Z. Ren (Eds.), Solid Propellant Chemistry, Combustion, and Motor Interior Ballistics, in: Progress in Astronautics and Aeronautics, vol. 185, AIAA, Reston, VA, 2000, pp. 689–722, P. Zarchan, Editor-in-Chief, Chapter 2.19.
[28] A.N. Zolotko, Ya.I. Vovchuk, N.I. Poletaev, A.V. Florko, I.S. Altman, Combust. Explos. Shock Waves 32 (3) (1996) 24–33.